Materials Chemistry and Physics 159 (2015) 25–37

Contents lists available at ScienceDirect

Materials Chemistry and Physics

journal homepage: www.elsevier.com/locate/matchemphys

Surface characterisation and photocatalytic performance of N-doped TiO_2 thin films deposited onto 200 nm pore size alumina membranes by sol–gel methods

R. Grilli [a, *], D. Di Camillo [b], L. Lozzi [b], I. Horovitz [c], H. Mamane [c], D. Avisar [c], M.A. Baker [a]

[a] The Surface Analysis Laboratory, Faculty of Engineering and Physical Sciences, University of Surrey, Guildford, Surrey, GU2 7XH, UK
[b] Dipartimento di Scienze Fisiche e Chimiche, Università degli Studi dell'Aquila, Via Vetoio, 67010 Coppito, L'Aquila, Italy
[c] School of Mechanical Engineering, Faculty of Engineering, Tel Aviv University, Tel Aviv 69978, Israel

HIGHLIGHTS

- Sol gel N-doped TiO_2 thin films were deposited on 200 nm pore size Al_2O_3 membranes.
- Two sol–gel methods have been compared – pipette drop and spiral bar deposition.
- The coatings showed a similar microstructure and composition but different morphology.
- The PCA (degradation of carbamazepine) was ~60% for both sol–gel coatings.
- The coated membranes are promising for use in a membrane based water treatment system.

ARTICLE INFO

Article history:
Received 31 July 2014
Received in revised form
23 January 2015
Accepted 27 March 2015
Available online 3 April 2015

Keywords:
Thin films
Oxides
Sol–gel growth
X-ray photoelectron spectroscopy (XPS)
Electron microscopy (SEM)

ABSTRACT

Membrane filtration is employed for water treatment and wastewater reclamation purposes, but membranes alone are unable to remove pollutant molecules and certain pathogens. Photocatalytically active N-doped TiO_2 coatings have been deposited by sol–gel onto 200 nm pore size alumina membranes for water treatment applications using two different methods, via pipette droplets or spiral bar applicator. The uncoated and coated membranes were characterised by X-ray photoelectron spectroscopy (XPS), scanning electron microscopy (SEM), X-ray diffraction (XRD) and energy dispersive X-ray spectrometry (EDX). Both coatings showed the presence of N-doped anatase, with a surface coverage between 84 and 92%, and nitrogen concentration (predominantly interstitial) of 0.9 at.%. The spiral bar applicator deposited coatings exhibit a thicker mud-cracked surface layer with limited penetration of the porous membrane, whilst the pipette deposited coatings have mostly penetrated into the bulk of the membrane and a thinner layer is present at the surface. The photocatalytic activity (PCA), measured through the degradation of carbamazepine (CBZ), under irradiation of a solar simulator was 58.6% for the pipette coating and 63.3% for the spiral bar coating. These photocatalytically active N-doped sol–gel coated membranes offer strong potential in forming the fundamental basis of a sunlight based water treatment system.

1. Introduction

The photocatalytic properties of titanium dioxide have been under investigation for over 50 years, and such properties make the material fit for an extensive number of applications, including solar cells [1], gas sensors [2], biomedical implants [3], anti-reflective coatings [4], self-cleaning surfaces and water and air purification [5,6]. Due to their band gap energies, anatase (3.2 eV) and rutile (3.0 eV) TiO_2 show photocatalytic behaviour under ultraviolet irradiation. In spite of its larger band gap, anatase is considered to be more photocatalytically active than rutile [7]. For the last 10 years, new methods have been proposed to extend the photocatalytic response to the visible region of the spectrum [8]. One of the common approaches, is doping TiO_2 with nitrogen [9]. This was first undertaken by Sato [10] and then some years later, Asahi et al.

* Corresponding author.
E-mail address: r.grilli@surrey.ac.uk (R. Grilli).

http://dx.doi.org/10.1016/j.matchemphys.2015.03.044
0254-0584/

reported on the photocatalysis of N-doped TiO_2 under visible light [11]. In the Asahi et al. paper, N-doped TiO_2 was prepared both as a powder and by reactive sputtering of a TiO_2 target. From the theoretical calculations of Asahi et al. [11,12] and Nakano et al., [13] N doping will result in a band gap narrowing due to the N 2p level mixing with O 2p states in the valence band. However, many other authors have proposed from theoretical and experimental studies that nitrogen doping leads to localised electronic states in the band gap and that the visible light activity arises from promotion of electrons from this inter-band state to the conduction band [8,14–16]. The specific origin of such inter-band states is a hotly debated topic (with reviews now appearing on the subject) and various authors have assigned their nature to different local solid-state nanostructures and defects, including substitutional N, interstitial N and oxygen vacancy based F-type colour centres [8,17].

Hu et al. and Peng et al. have prepared N-doped TiO_2 films using different sol–gel methods [18,19]. In both papers, the presence of N and its chemical state was investigated by XPS analysis. Their results have shown that the location of N within the TiO_2 structure and the thin film photocatalytic activity are influenced by the preparation method [18,19]. Hu et al. obtained a film containing interstitial N and another containing both interstitial and substitutional N, with the second showing the highest photocatalytic activity (PCA). Peng et al. also demonstrated that interstitial nitrogen doping produces higher visible light activity than substitutional nitrogen [19]. The authors attributed this result also to the higher overall N content and concentration of oxygen vacancies. In other work on sol–gel deposited thin films, Quiao et al. have reported on a triethanolamine assisted sol–gel preparation of monodisperse sub-micron size N-doped TiO_2 hollow spheres. The authors found that increasing the N content shifted the optical response more to the visible light region and this could be controlled through varying the amount of triethanolamine employed [20].

The PCA is also directly dependent on the grain size, with an increase in the grain size corresponding to an increase in activity [7,21]. The grain size, crystallinity and microstructure of the film are dependent on the calcination temperature and pH of the sol–gel solution [22,23]. Co-precipitation of TiO_2 with urea followed by thermal treatment is one of the most common methods to prepare sol–gel deposited N-doped TiO_2 [24–26], however the doping mechanism is still not very clear. A study of these mechanisms was undertaken by Factorovich et al. [27], who highlighted the importance of by-products generated during thermal decomposition of the urea. Azoani et al. studied doped nanocoatings (comprised of particles with a radius <3 nm and small size distribution) formed from chemically active TiO_2 colloids, and demonstrated that doping of smaller units leads to higher PCA [28].

There are only a few studies of membranes coated with a photocatalyst layer for water treatment purposes reported in the literature. The most relevant recent work by Ma et al. reports on a Si-doped TiO_2 sol–gel coating deposited onto a tubular 200 nm pore size alumina membrane [29]. The Si-doped TiO_2 layer exhibited an anatase structure with a grain size of 8–10 nm. Increasing the sol–gel coating thickness reduced the water permeability through the membrane with 2 coating cycles reducing the water permeability by 45%, indicating that the pore size had decreased substantially through deposition of the coating. In PCA tests under UV irradiation, the concentration of a commercial reactive azo dye (RR ED-2B) was reduced by almost 40% after 40 min of irradiation. Longer irradiation times did not increase the amount of dye removed. Choi et al. have also deposited a sol–gel TiO_2 coating onto a 'home made' 100 nm pore size alumina membrane [30]. They showed that the TiO_2 sol–gel film could be successfully deposited onto the alumina membrane and exhibited high water permeability and effective organic matter retention. No PCA results for the coated membranes were reported, but 8–10 nm grain size TiO_2 thin films on glass prepared by the same sol–gel method were effective at degrading methylene blue and creatinine under UV light irradiation. Approximately, 60% of the creatinine was degraded after 14 h of irradiation [30].

Photocatalytic processes involve the initial absorption of photons by the substrate to produce electron–hole pairs. The photocatalytic oxidation of an organic species often proceeds via adsorption of the pollutant on the surface of the catalyst, followed by direct removal of electrons from the pollutant molecule by positively charged holes. Another possible oxidation process is through hydroxyl radical ($OH^{\bullet}$) attack of the pollutant, which takes place at the photocatalyst surface or in its vicinity.

Carbamazepine (CBZ) is used to relieve neuralgia and to treat seizure and mental disorders. CBZ has been detected in wastewater [31–33], surface water [34–36] and groundwater [37,38]. The compound has shown little degradation or retention during bank filtration [34,35] or in sediment-transport studies [39–41]. CBZ is a relatively polar, neutrally charged pharmaceutical and lacks sites for specific interactions with soils and sediments, which leads to its non-appreciable sorption properties [42–44]. CBZ is a neutral molecule over a broad range of pH values, and therefore photocatalysis is affected by pH via the surface charge of the photocatalyst. Vogna et al. [45] investigated the advanced oxidation process (AOP) of CBZ with UV/H_2O_2 and found that CBZ degradation by radical-induced reaction is not affected by changing the pH of the solution in the range of 2.0–8.0. This compound is ideal for photocatalytic experiments due to its unique physico-chemical characteristics together with the fact that many studies have already used this compound as a hydrophilic and persistent marker to trace anthropogenic pollution [41,46].

In this work, a sol–gel method was developed to deposit photocatalytically active thin films of N-doped TiO_2 onto Al_2O_3 membranes with a pore size of 200 nm. Membranes with a photocatalytically active coating are being considered for use in sunlight stimulated water treatment systems. The sol–gel solution was deposited on the membrane through the use of manual pipette droplets or a spiral bar applicator followed by annealing at 450 °C to form a crystalline coating. The coated membranes were characterised by X-ray photoelectron spectroscopy (XPS), scanning electron microscopy (SEM), X-ray diffraction (XRD) and energy dispersive X-ray spectrometry (EDX). The PCA was measured through monitoring the degradation of CBZ in a solution with a pH value of 7. The PCA measurements were performed in a flow cell using a solar simulator as a light source. The membrane permeability before and after sol–gel coating was also determined.

2. Experimental

2.1. Film preparation

The N-doped TiO_2 coatings were prepared by sol–gel deposition using tetrabutylorthotitanate, isopropanol, ammonium hydroxide and triethanolamine as precursors. Tetrabutylorthotitanate (25 mL) and triethanolamine (15 mL) were dissolved in isopropanol (32 mL), together with ammonium hydroxide (32%, 2.4 mL) [47]. After stirring vigorously for 30 min at room temperature, the solution was ready for use. The substrates were Al_2O_3 membranes (KSM Water GmbH, Germany) with a nominal pore size of approximately 200 nm. Before the solution was deposited, the substrates were carefully cleaned by ultrasonic treatment with citric acid in water solution (g/L, at 80 °C) and then in acetone (at room temperature), and finally air-dried for 24 h. The N-doped TiO_2 coatings were prepared by two different methods: (a) a drop-

coating method using a pipette (2.5 mL drops); (b) using a spiral-bar applicator. In the spiral bar method the membrane was placed on the flat surface of the spiral bar applicator (by TQC, Italy, model AB3220). The spiral bar, wound with a stainless steel wire (10 μm thick) was carefully placed at one end of the membrane, and was in contact with the membrane surface. The solution was deposited onto the membrane by means of a pipette adjacent to the spiral bar. Immediately after the bar moved across the surface at a fixed speed (5 mm/s) spreading the solution over the membrane. In both cases the composition and preparation method for the sol–gel was identical. After sol gel deposition, the coated membranes were annealed in an oven for 1 h at 450 °C in air.

2.2. Surface characterization

XPS analysis was performed using a Thetaprobe spectrometer (by ThermoFisher Scientific East Grinstead, UK), using an Al Kα monocromated radiation at a power of 140 W, a spot size of 400 μm and a take off angle of 37° (with respect to the surface normal). The survey spectra were acquired over a binding energy range of 0–1350 eV using a channel width of 0.4 eV and a pass energy of 300 eV. High resolution elemental XPS were acquired using a 0.2 eV channel width and 50 eV pass energy. The aliphatic C peak at 285.0 eV was used as a binding energy reference. Curve fitting was undertaken with the ThermoFisher Scientific Avantage software after subtraction of a Shirley background and quantification performed using instrument modified Wagner sensitivity factors.

The SEM micrographs were acquired with a Quanta FEG 200 microscope (by FEI, Eindhoven, The Netherlands), operating at a beam voltage of 20–30 kV, 30 μm aperture and spot size 3 for high resolution imaging. According to the need, the sample was tilted up to 20°.

XRD spectra were acquired using a X'Pert Pro diffractometer (by Panalytical, Cambridge, UK). The Cu Kα radiation (λ = 1.5406 Å) source was operated at 40 mA and 45 kV. The 2Θ range acquired was 10–65°, employing a channel width of 0.017 2Θ. The average grain size was determined using the Scherrer equation (equation (1)):

$$D = \frac{k\lambda}{\beta \cos\theta} \quad (1)$$

where D is the average crystallite size (Å), k is the shape factor (taken as 0.9), λ is the wavelength of the X-ray radiation and β is the peak full width half maximum (FWHM), and θ is the Bragg angle of the peak. It was assumed that peak broadening is entirely due to grain size effects.

2.2.1. Calculation of the substrate coverage

The coverage of the Al_2O_3 substrate by the TiO_2 film was calculated from the atomic percentages of titanium and aluminium, obtained by XPS, and normalized by the atomic densities D in the two solids:

$$Coverage = \frac{at\%\ Ti/D\ (TiO_2)}{at\%\ Ti/D(TiO_2) + at\%\ Al/D(Al_2O_3)} \times 100 \quad (2)$$

The atomic densities were calculated as follows:

$$D = \frac{n \times Z}{V} \quad (3)$$

where n is the stoichiometric coefficient, Z is the number of chemical formula units per unit cell, and V is the volume of the primitive cell. The anatase TiO_2 has n = 1, Z = 4 and a cell volume V of 1.3631×10^{-22} cm^3 [JCPDS no. 00-021-1272]; the α-Al_2O_3 has n = 2, Z = 6 and a cell volume of 2.5481×10^{-22} cm^3 [JCPDS no. 00-046-1212]. The resulting atomic densities are 4.71×10^{22} atoms × cm^{-3} for the alumina, and 2.93×10^{22} atoms × cm^{-3} for the titania.

Atomic force microscopy (AFM) was performed using a Solver, HV MFM (by NT-MDT, Moscow, Russia). Phase maps were produced via tapping mode in ambient conditions using silicon tips with a mean frequency 323 kHz and k = 32–60 N/m.

2.3. PCA test

2.3.1. Materials and equipment

Carbamazepine (CBZ) was employed as the target pollutant for the PCA tests. CBZ (>99% purity) was obtained from Sigma–Aldrich.

The feed solution containing CBZ (DI water adjusted to pH 7) was diluted from a stock solution to an initial concentration of 1 mg/L, 4.24×10^{-6} M. Experiments were carried out at neutral pH (7) adjusted using 1 mM phosphate buffer saline (Na_2HPO_4/NaH_2PO_4).

2.3.2. Experimental procedure

A 300 W ozone-free xenon arc lamp (Newport, full spectrum 300 W, 50.8 mm × 50.8 mm, CT, USA) was used with a maximum optical output irradiance given by the manufacturer of 2000 W/m^2 (2 suns) after the light beam was filtered with a 1.5 Global air mass (AM) filter. The incident spectral irradiance was measured by a calibrated spectroradiometer (International light, ILT 900R, USA) with a horizontal detector. The integrated irradiance was 1.4 W/m^2 for the UVB range (280–320 nm), 55.0 W/m^2 for the UVA range (320–400 nm) and 712.3 W/m^2 for the visible range (400–700 nm).

The coated membrane PCA was determined by a custom-made, versatile laboratory flow cell as detailed in Fig. 1. The flow cell is a bench-scale system used for concurrent filtration and solar photocatalytic degradation used in semi-batch operation mode. The flow cell was placed underneath the solar simulated light. The filtered and irradiated area of the filtration cell was 43.6 × 21.6 mm. A quartz cover was placed above the membrane to ensure a uniform water height above the membrane of 6.5 mm and acted as the chamber seal. A 200 mL feed solution of CBZ (1 mg/L, pH 7), was recirculated for 30 min through the system to ensure an adsorption/desorption equilibrium of CBZ on the membrane prior the irradiation. The feed solution was then filtered through the flow cell (from the bottom-up) to the photocatalytic coated side of the membrane in a dead end filtration mode (see Fig. 1). Hence, only the permeate was exposed to the effects of photocatalysis. The treated water was collected at the permeate side and pumped back to the feed bottle after each cycle, for a total irradiation time of 2 h. Samples were collected between cycles and analysed using high performance liquid chromatography (HPLC). The filtration flow rate during the experiment was 0.5 L/h, achieved using a compressed air line connected to a sealed feed bottle at a pressure of 0.1 bar.

Carbamazepine (CBZ) was detected and quantified using an Agilent, model 1100 HPLC instrument. The selected liquid chromatograph column was a Phenyl Reverse Phase column (ACE-RP, 2.1 mm × 250 mm, 5 μm). The mobile phase consisted of water (A) and methanol (B) and the detection wavelength was 286 nm. The flow rate was set to 0.5 mL/min and the injected volume was 100 μL. The mobile phase eluent gradient started with 60% of eluent A, followed by a 2-min linear gradient to 10% eluent A, 4-min isocratic elution and a 2-min linear gradient back to 60% of eluent A, maintained for 5 min to equilibrate.

The photocatalytic efficiency was expressed as percent removal:

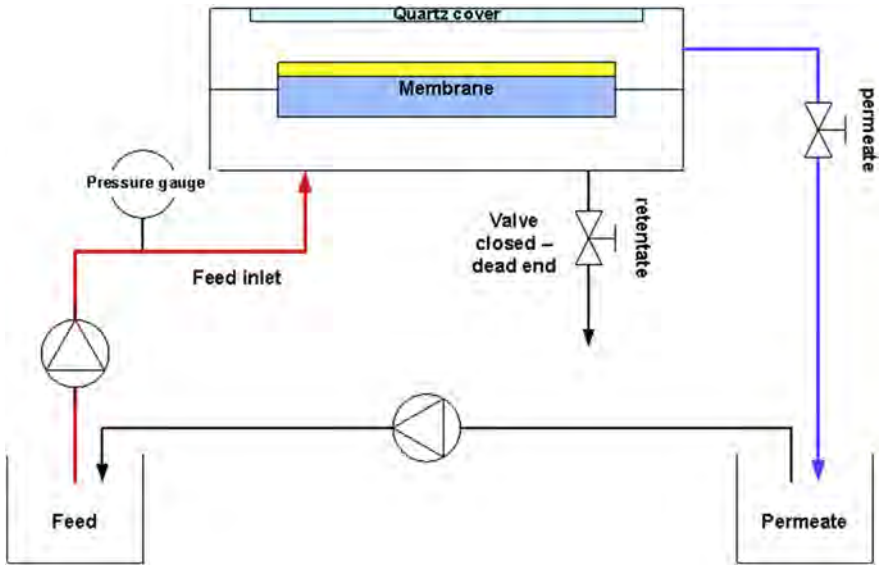

Fig. 1. A schematic diagram of the bench-scale system used for concurrent filtration and solar photocatalytic degradation – semi-batch operation mode.

$$\text{Removal } (\%) = \frac{C_0 - C_t}{C_0} \times 100 \quad (4)$$

where C_0 is the initial pollutant concentration after equilibrium and C_t is the pollutant concentration after t hours of irradiation (mg/L).

The flow cell is operated at semi-batch mode with a retention time calculated to be ~4 min by the following equation:

$$t_R = \frac{V_{illu}}{V_t} \times t \quad (5)$$

where t_R is the retention time (min); V_t is the total volume (200 mL); t is the experiment time (120 min); V_{illu} is the volume of illuminated section of each module (mL). V_{illu} is equal to the membrane area A (9.42 cm^2) multiplied by water height h (0.65 cm), which is 6.12 cm^3, or 6.12 mL.

The water permeability was determined by measuring a pure water flux in a pressure step test experiment. Nitrogen (99.999%) was used to force deionised water from a 5 L holding tank into the membrane pressure cell by dead end filtration. The accumulated permeate water weight with time, J, was recorded using 'Balint' software and calculated using Equation (6).

$$J = \frac{Q}{A} = \frac{\Delta m}{\rho \Delta t \frac{1}{60} A} \quad (6)$$

Where J is the flux [L/(m^2*h)], Q is the filtrate flow [L/h], A is the membrane surface area [m^2] and ρ is the water density (determined from the average water temperature during the experiment).

3. Results

3.1. Surface characterisation

3.1.1. Alumina membrane

The substrate supplied by KSM Water GmbH, Germany, is a Al_2O_3 membrane with 200 nm pore size used for water filtration. An SEM cross-section image of the membrane is given in Fig. 2 and shows the presence of a surface layer of approximately 10–15 μm in thickness, which is acting as the finer 200 nm pore size filter.

Fig. 3a, b and c show SEM micrographs at different magnification of the membrane surface. The membrane appears to have a homogeneous structure over a large area, with particle sizes ranging from sub-micron to a few micrometres in size. Fig. 3b also shows the presence of smaller particulates of tens to hundreds of nanometres in size decorating the larger grains. However, it should be noted that the presence of these smaller particulates decorating the surface only occurred on some areas of the membrane and in this respect the membrane surface was inhomogeneous. A higher magnification SEM image showing these small particulates in more detail is given in Fig. 3c. This SEM micrograph in Fig. 3c has a field of view of approximately 2 × 2 μm, and can be compared with the AFM phase analysis image (Fig. 3d), which has a similar field of view, but is taken from a different area on the same surface. It is clear from the AFM image that two distinct phases are present, with the localised bright features in the image corresponding to particulates present on the surface of the second phase (darker background). The size and distribution of the small particulates in the AFM phase image is in agreement with the distribution of the small particulates observed in the SEM image.

XRD was performed to investigate the phase composition of the membrane (Fig. 4). The high intensity peaks correspond to the presence of the α-Al_2O_3 phase [JCPDS no. 00-046-1212]. A ZrO_2 phase was also present [JCPDS no. 00-037-1484] and a third phase was also observed, attributed to mixed Al/Zr oxide [JCPDS no. 00-053-0294] The average grain sizes for the different phases was calculated to be 96 nm (Al_2O_3), 34 nm (ZrO_2), and 57 nm (Al/Zr mixed oxide). This would indicate that the larger alumina particles are polycrystalline and the small particulates on the surface of the larger alumina grains in Fig. 4 may be any of these three phases. The presence of small grains of ZrO_2 or mixed Al/Zr oxide on the surface of the larger Al_2O_3 grains would be consistent with the AFM phase image results in Fig. 3. The presence of zirconium was confirmed by EDX analysis, which showed a Zr concentration of about 1%.

3.1.2. Pipette deposited N-doped TiO_2 sol–gel coating on alumina membrane

A low magnification SEM micrograph (Fig. 5a) of the membrane surface after deposition of the sol–gel N-doped TiO_2 coating shows a surface very similar to the uncoated membrane (Fig. 3a), with the

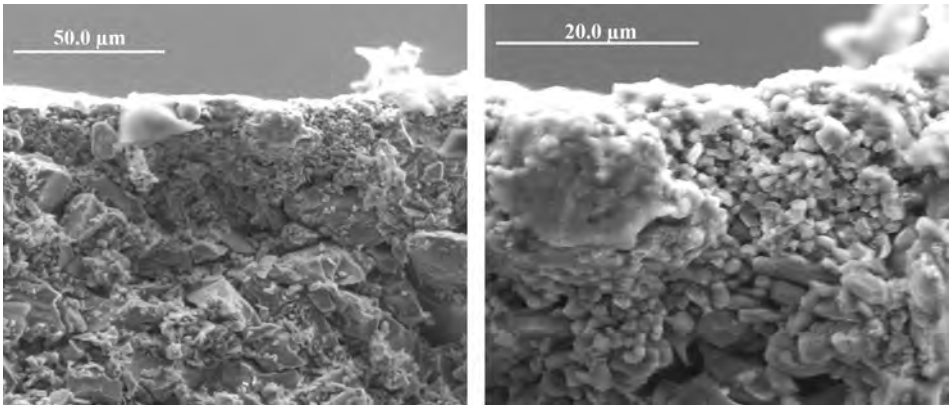

Fig. 2. SEM cross section micrographs of the Al_2O_3 membrane showing the presence of the 200 nm pore size layer at the surface with a thickness of approximately 10–15 µm.

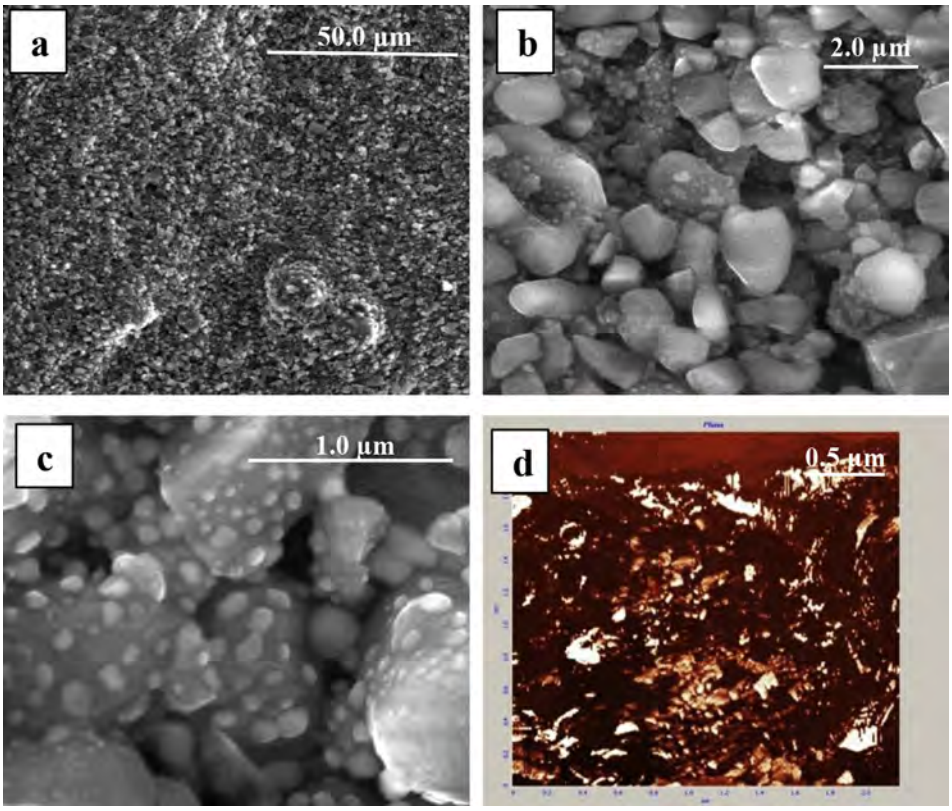

Fig. 3. (a), (b) and (c): SEM micrographs of the membrane surface at different magnifications; (d) AFM phase analysis of the membrane surface with the same magnification as the SEM image in (c), but from a different area on the surface.

alumina particles and pores being evident. At higher magnification (Fig. 5b), there are again island features present on the larger alumina grains, somewhat similar to those seen on the uncoated membrane (Fig. 3b), but the density of these features is higher on the coated membrane (Fig. 5b) and their form is globular rather than the obvious particulate nature of the features in Fig. 3b. This is apparent from the regions marked with arrows, where a number of globules appear to have coalesced, forming larger more irregular shaped 'islands'. Fig. 5c shows another high resolution micrograph with the same magnification, but from a different region on the same membrane surface. In this Figure there are no small rounded particulates/globules, but instead the presence of sharp-edged, crystalline type particulates. Hence, it is difficult to specifically identify the morphology of the N-doped TiO_2 coating on the membrane surface (even though it will be shown from the XRD results (Fig. 4) and the XPS determined surface composition (Table 1) that the sol–gel coating is present on the surface. Fig. 5d shows an AFM phase image of the surface, with a field of view of 2.5×2.5 µm taken from a different area on the surface to either of the 2 SEM high resolution images in Fig. 5. The image indicates the presence of two phases, one phase distributed over the surface of a matrix phase. In the case of the uncoated membrane (Fig. 3c and d) there was a dominant matrix phase (the alumina) and the second phase was present as small particulates on the surface. In this case, for the coated membrane, the distribution of the surface phase is very different, being more evenly spread over the underlying

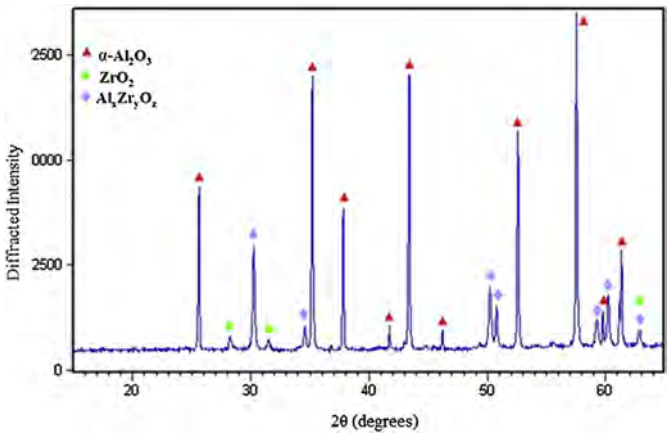

Fig. 4. XRD pattern of the 200 nm pore size membrane.

matrix. It seems probable that the image represents the N-doped TiO_2 coating distributed over the underlying Al_2O_3 membrane, showing that the N-doped TiO_2 film is not a continuous and uniform coating on the surface, but exhibits a fairly good surface coverage of the membrane.

The XRD pattern for the pipette deposited coating on the membrane is shown in Fig. 6. There are many peaks confirming that the N-doped TiO_2 coating is present on the surface in the form of anatase. The average grain size, calculated from the (200) reflection, is 12 nm. The other XRD peaks present correspond to alumina, zirconia and the mixed Al–Zr oxide phase, as seen for the uncoated membrane.

The XPS determined chemical composition of the surface is given in Table 1. The Ti $2p_{3/2}$ peak is at a binding energy (BE) of 458.8 eV, corresponding to TiO_2 and the Al 2p peak occurs at a BE of

Table 1
XPS determined surface composition (at.%) and peak binding energies (eV) for the pipette deposited N-doped TiO_2 coating on the membrane.

XPS peak	C 1s	O 1s	Ti 2p	Al 2p	Zr 3d 3d3d	Mo 3d	N 1s
Concentration (at.%)	12.6	62.7	18.2	5.1	0.4	0.2	0.9
Binding Energy (eV)	285.0	–	458.8	74.3	182.2	231.7	–

74.3 eV, corresponding to Al_2O_3. The XPS Ti and Al concentrations are determined to be 18.2 and 5.1 at.% respectively confirming that there is non-conformal coverage by N-doped TiO_2 coating and that the membrane is partially exposed. This is in good agreement with the AFM phase image results in Fig. 5d.

An estimate for the surface coverage can be made from the XPS Ti and Al concentrations using the formula Ti/(Ti + Al), where the Ti and Al elemental concentrations have been normalised to take into account the Al_2O_3 and TiO_2 unit cell volumes and atomic number densities of Ti in TiO_2 and Al in Al_2O_3. The surface coverage values calculated in this way do not take into account any local variations in the thin film coverage or the specific active surface area exposed (e.g. due to high surface roughness or porous structure). Hence, the limitations of this approach should be noted, but, the values provide a useful indicator of relative surface coverage between different coatings. The results show that there is an approximate surface coverage of 84% for the pipette deposited N-doped TiO_2 coating on the membrane.

The XPS O 1s peak, shown in Fig. 7a is comprised of three components. Peak 1 (BE = 530.0 eV) corresponds to TiO_2, peak 2 (BE = 531.2 eV) corresponds to Al_2O_3 and the surface OH^- groups and peak 3 (BE = 532.5 eV) can be attributed to adsorbed water. Sol–gel deposited coatings are known to be partially hydrated and the presence of OH^- peaks in the XPS spectra from such coatings is common [48].

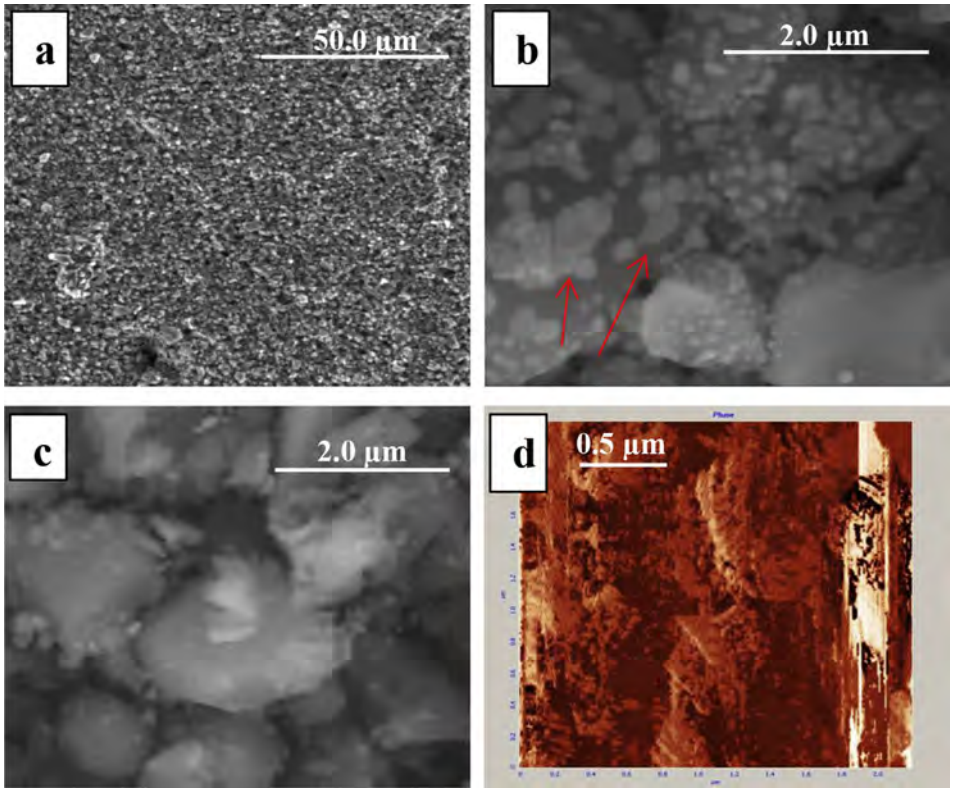

Fig. 5. a, b, c, SEM micrographs of the surface of the N-doped TiO_2 pipette coated membrane at different magnifications; d, AFM phase analysis with 2.5 × 2.5 µm field of view.

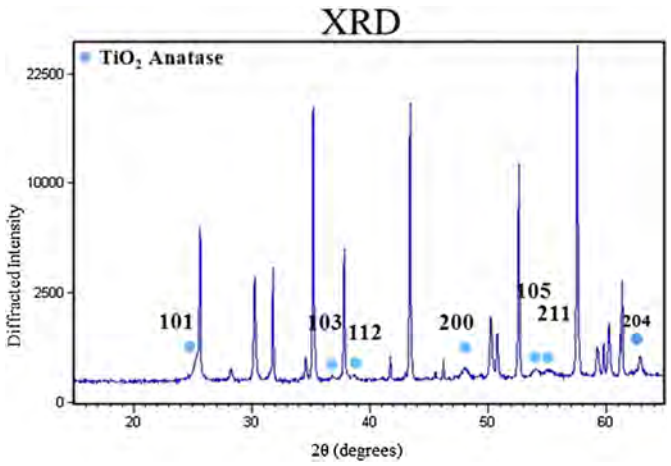

Fig. 6. XRD pattern for the pipette deposited N-doped TiO_2 sol–gel coating on the membrane.

The nitrogen concentration present on the surface was 0.9 at.%. The N 1s photoelectron peak, shown in Fig. 7b, could be fitted with 4 peaks, each contributing 0.1–0.3 at.% N (see Table 2). There is also a small contribution at the same binding energy from the Mo $3p_{3/2}$ peak. The origin of the N 1s peak components in N-doped TiO_2 has been much discussed in the literature. However, it is generally accepted that a N component at approximately 396 eV corresponds to N substituted for O in the TiO_2 phase [12,49–57]. It has recently been shown that a peak at approximately 400 eV is observed on many surfaces due to the presence of N-containing organic contamination [58], but a peak can also occur at a similar binding energy due to the presence of interstitial NO species [49,52,59–62]. Furthermore, the peak at approximately 402 eV is associated with surface contamination [58]. (It should be noted that on the uncoated surfaces, the N 1s peak for both the 200 nm membranes showed the presence of one component, at approximately 400 eV). The final component, at approximately 398 eV most probably corresponds to interstitial N in the TiO_2 phase [12,63–65]. Hence, in the N-doped TiO_2 thin film on the 200 nm membrane, N is present as both substitutional and interstitial N (and possibly interstitial NO).

EDX analysis of the pipette deposited N-doped TiO_2 coated membrane showing the surface composition is given in Table 3. It should be noted that due to the roughness of the coated membrane surfaces, these quantified EDX values should only be considered as indicative. Spectra were acquired from three different points on the surface and the chemical composition was found to be fairly homogeneous. The average composition values are presented in Table 3. The low concentration of Ti indicates the presence of a thin coating, which is in agreement with the XRD results and the difficulty in observing a distinct coating morphology at the surface with SEM. The presence of Zr is also consistent with the XRD results showing ZrO_2 and mixed Al/Zr oxide particles present on the membrane surface.

Table 2
XPS N 1s peak fitted components (corresponding to Fig. 7 (b)) for the pipette deposited N-doped TiO_2 coating on the 200 nm pore size membrane.

XPS N 1s component	1	2	3	4
Concentration (at%)	0.2	0.3	0.2	0.1
Binding Energy (eV)	396.1	398.1	400.1	402.0

Table 3
EDX determined surface composition of the N-doped TiO_2 coating deposited on the membrane by pipette and spiral bar sol–gel deposition.

Element	C	O	Ti	Al	Zr
Pipette	1.5	64.3	1.5	31.9	0.8

3.1.3. *Spiral bar deposited N-doped TiO_2 sol–gel coating on alumina membrane*

SEM images of the spiral bar deposited N-doped TiO_2 coating on the alumina membrane are presented in Fig. 8. The surface exhibits a very diffierent morphology to that obtained through pipette sol–gel deposition. Use of the spiral bar applicator results in a much thicker coating being deposited, with the coating showing a 'mud-cracked' morphology (Fig. 8a and b). This morphology is often observed for sol–gel deposited coatings [66]. In this case, the thicker coating can be clearly distinguished from the underlying membrane. The coating varies in thickness across the surface, with the thicker regions showing larger and more discernible cracks at low magnifications (Fig. 8a). At higher magnifications (Fig. 8b and c), the underlying membrane can be observed through the cracks. Smaller particulates can also be observed on the membrane surface (Fig. 8c and d) similar to those seen on the uncoated membrane (Fig. 3b). The formation of the 'mud-cracked' morphology, leaving some area of the membrane exposed is clearly important in allowing water to pass through the membrane.

Fig. 9 shows the XRD pattern of the N-doped TiO_2 coated membrane, with the labelled reflections corresponding to the anatase phase. The diffraction pattern is very similar to that obtained for the pipette deposited N-doped TiO_2 coating on the membrane (Fig. 6), but the anatase peak intensities are stronger, consistent with the presence of a thicker coating. The grain size,

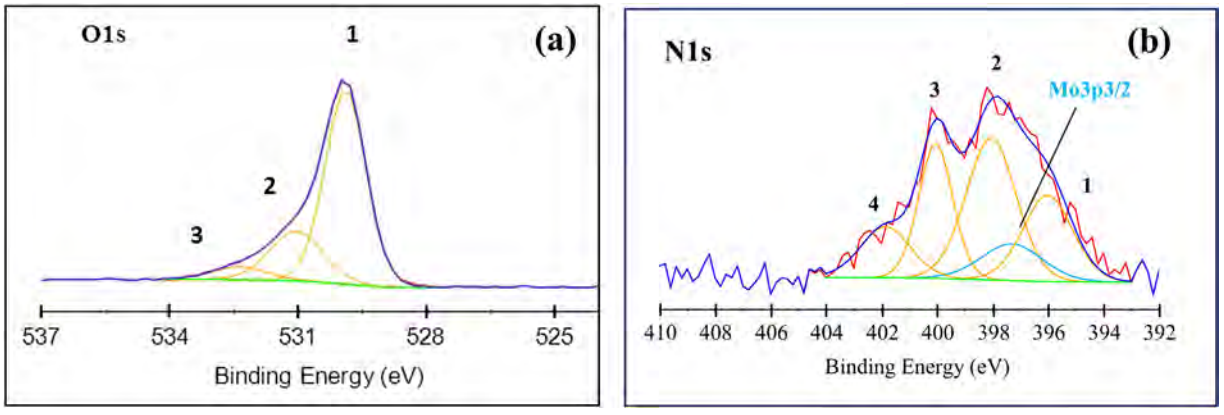

Fig. 7. XPS spectra from the pipette deposited N-doped TiO_2 sol–gel coating on the membrane. (a) O 1s peak; (b) N 1s peak.

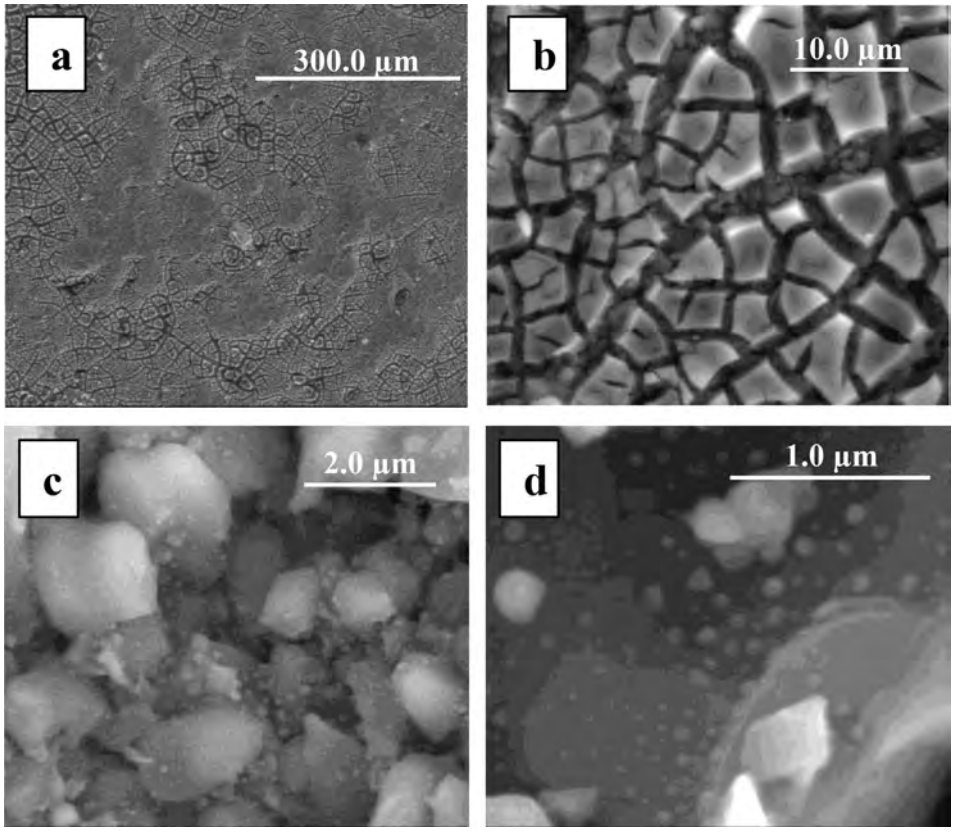

Fig. 8. SEM micrographs N-doped TiO_2 sol–gel coatings deposited on the membrane by spiral bar applicator.

calculated from the (200) reflection, is 16 nm. As for the pipette deposited coating on the membrane, the other reflections correspond to alumina and zirconia, and the mixed Al/Zr oxide phase.

Table 4 shows the surface composition of the coated membrane, determined by XPS. The Al concentration is lower than that found for the pipette deposited coating, indicating a greater coverage of the membrane using the spiral bar applicator. The surface coverage of the membrane, was estimated by XPS to be 92%, which is consistent with the SEM results. The surface concentrations of O and N for the pipette and spiral bar deposited coatings on the membrane are very similar and the curve fits of the O 1s and N 1s spectra are presented in Fig. 10. The XPS O 1s and N 1s peakshape

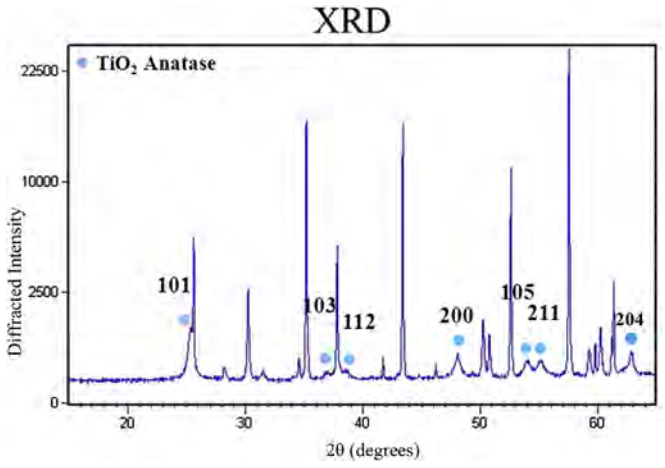

Fig. 9. XRD pattern of the spiral bar applicator deposited N-doped TiO_2 sol–gel coating on the membrane.

Table 4
XPS determined surface composition (at.%) and peak binding energies (eV) for the spiral bar deposited N-doped TiO_2 coating on the membrane.

XPS peak	C 1s	O 1s	Ti 2p	Al 2p	Si 2p	Zr 3d	Mo 3d	N 1s
Composition (at%)	13.3	61.3	19.8	2.6	1.9	0.3	0.1	0.8
Binding Energy (eV)	285.0	–	458.8	74.8	103.3	282.6	231.4	–

are remarkably similar to those observed for the pipette deposited coating (Fig. 7) and consequently the interpretation of each of the O 1s and N 1s components is the same as that for the pipette deposited coating, given in section 3.1.2.

EDX point analysis results taken from one of the large N-doped TiO_2 islands on the mud-cracked surface, marked as point 1 in Fig. 11a, is given in Table 5. Considering the analysis depth of EDX, the high concentration of Ti (24.9 at.%) and low concentration of Al (2.4 at.%) would suggest that for the largest islands, the spiral bar applicator deposited coating has a thickness which is greater than 1 µm. Spectra taken from islands where the coating was clearly thinner (e.g. point 3 in Fig. 11b), showed Ti concentrations reducing to around 4 at.%. Hence, the average coating thickness is then probably of the order of several hundred nanometres. EDX point spectra were also taken from within the cracked region, marked as point 2 in Fig. 11a, and a small Ti concentration was observed, indicating that there is some sol–gel coating present also within these cracked regions.

3.2. Photocatalytic activity

Photocatalytic degradation of 1 mg/L CBZ was carried out using sol–gel N-doped TiO_2 coated Al_2O_3 membranes deposited either by pipette or by the spiral bar applicator. Direct photodegradation of

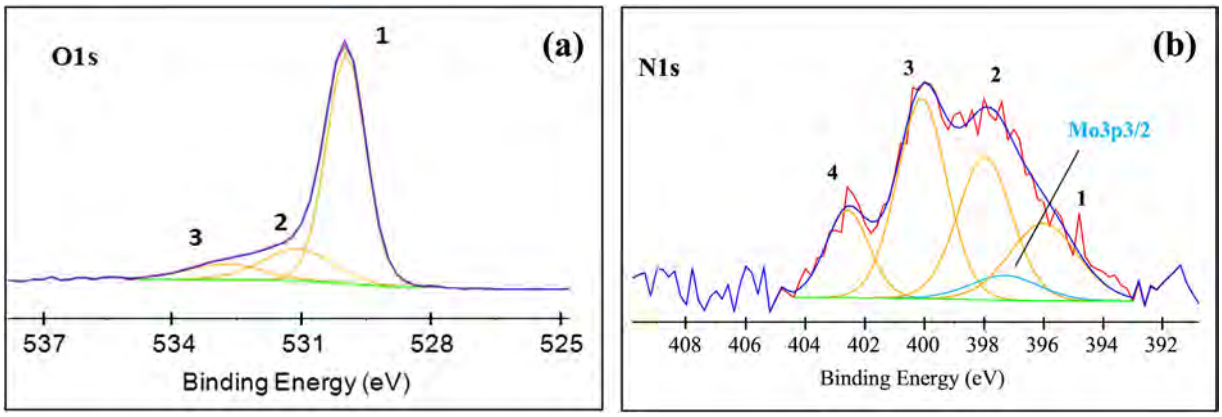

Fig. 10. XPS spectra from the spiral bar applicator deposited N-doped TiO_2 sol–gel coating on the membrane. (a) O 1s peak; (b) N 1s peak.

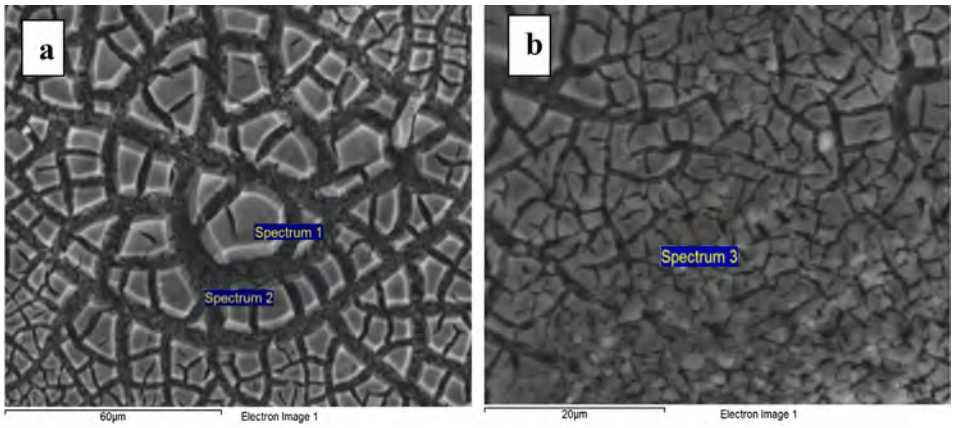

Fig. 11. SEM images of the spiral bar deposited N-doped TiO_2 coating (EDX analysis points marked on the image).

Table 5
EDX determined surface composition of the N-doped TiO_2 coating deposited on the membrane by spiral bar sol–gel deposition.

Element	C	O	Ti	Al	Zr
Point 1	2.9	69.8	24.9	2.4	–
Point 2	–	58.7	9.2	30.1	2.0
Point 3	5.4	60.5	4.5	28.8	0.8

CBZ (in the presence of an uncoated Al_2O_3 membrane) after 120 min exposure was negligible (<1%). Furthermore, CBZ showed negligible adsorption to the N-doped TiO_2 coated membranes when exposed in the dark. After 120 min, both deposition techniques show similar CBZ degradation rates of 63.3% removal for the spiral bar applicator coated membranes and 58.6% removal for the pipette coated membranes (Fig. 12). In a recent study undertaken by the authors, conducted on the same alumina membranes with a pore size of 800 nm, a comparison of CBZ degradation for doped and undoped TiO_2 was conducted. The N-doped TiO_2 resulted in significantly higher removal rate (by ~40%) compared to the undoped TiO_2 coated membranes with removal of 63% and 38% respectively, after 120 min of experimental duration (Fig. 13), confirming that the doping process would extend the photocatalytic response to the visible portion of the spectrum. These PCA results were shown to be repeatable to within 5%.

In this study, the PCA was examined in a phosphate buffer solution, however in a previous study, the PCA of the same coatings on glass slides showed a dependence on various water quality parameters such as pH, alkalinity, natural organic matter, etc [47].

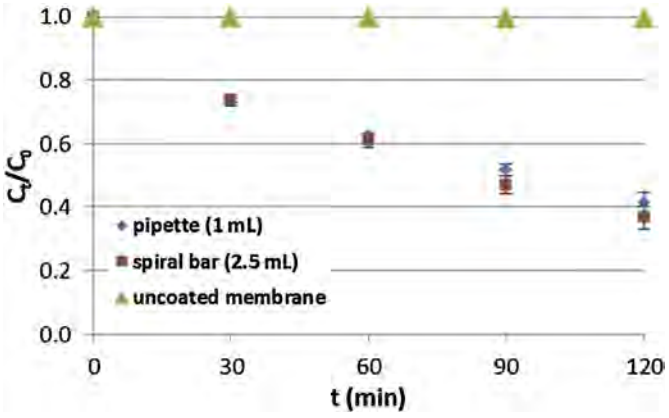

Fig. 12. CBZ removal as a function of time using uncoated (Δ), spiral bar applicator deposited N-doped TiO_2 coated (□) and pipette deposited N-doped TiO_2 coated (◊) membranes.

Recirculating the CBZ solution on top of the coated membrane resulted in significantly lower reaction rates, by ~90% compared to flow through the coated membrane pores. Flow through the coated porous membrane is advantageous as opposed to flow on top of the membrane due to the considerably higher available photocatalytic surface area and increase in direct contact between the solution and membrane surface due enhanced mixing conditions.

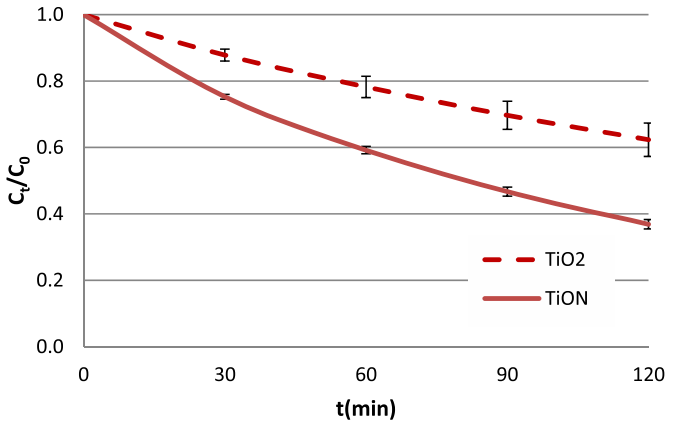

Fig. 13. CBZ removal by N-doped TiO_2 and TiO_2 coated membranes (800 nm pore size) under solar simulator light.

3.3. Water permeability

Permeability of the uncoated and coated 200 nm membranes was measured to evaluate the integrity and properties of the membranes before and after deposition of the sol–gel coating. The water permeability for the uncoated 200 nm membrane was found to be 3800 ± 17% L/m^{2}h/bar. The values for the pipette and spiral bar applicator coated membranes were determined to be 1600 ± 20% and 2100 ± 28%. The variation in values recorded for either the pipette or spiral bar applicator coated membranes indicate that there is no significant difference between the two coating methods, both giving a reduction in the water permeability of approximately 50% compared to the uncoated membrane. The variability in the water permeability results for both the uncoated and coated membranes probably arises from an inconsistent pore size distribution for the membrane.

4. Discussion

Surface characterisation of the sol–gel coated membranes has shown that the pipette and spiral bar applicator deposited N-doped TiO_2 coatings have different morphologies and thickness, but very similar crystal structure (small difference in grain size), N doping and surface coverage. The sol–gel process is clearly capable of forming coatings which are reproducible in terms of crystal structure and N doping and it is the method of applying the sol–gel which is giving rise to the variations in morphology and thickness observed. Using the spiral bar applicator results in the sol–gel remaining at the surface, with little or no penetration into the pores, whereas depositing the sol–gel through a pipette drop method allows the sol–gel solution to penetrate the pores. The extent of penetration of the sol–gel solution in the porous membrane is the result of capillary pressure and gravity. The capillary pressure has a similar effect for both methods, as the surface tension of the solution and the wettability of the substrate are the same in both cases. The discriminating factor is the pressure due to gravity. With the pipette method, the solution was deposited as individual drops of 2.5 mL equally spaced across the membrane surface, while with the spiral bar applicator the same amount of solution was distributed across the surface giving a continuous film with a thickness of several microns. As an individual drop would have a diameter of at least a few millimetres the applied force per unit area due to gravity would be higher than for a thin film being evenly spread over the surface by the spiral bar applicator. There could also be an additional downward pressure arising from acceleration of the drop towards the substrate surface, due to gravity (depending on the distance of the pipette from the substrate) or due to the pressure applied to the sol–gel solution in the pipette to release the drop. To summarise, with the pipette method there is additional downward pressure given to the solution to penetrate the pores of the alumina membrane, compared with the spiral bar method, where the solution is gently spread across the surface.

The observed 'mud-cracked' thick morphology for the spiral bar applicator deposited coating is typical for sol–gel deposited coatings generated after annealing and cooling and occurs due to the different thermal expansion coefficients of the TiO_2 sol–gel coating and Al_2O_3 membrane.

The similar CBZ removal rates for coatings deposited by each method would suggest that the crystal structure and N doping are the most important factors affecting PCA, whereas the variation in coating thickness and morphology is not having a significant effect. The small increase in the PCA observed for the spiral bar applicator deposited coatings may be attributable to a slightly higher surface coverage of the membrane by these coatings compared to the pipette deposited coatings. Both sol–gel deposited coatings exhibit a pure anatase TiO_2 structure, which is generally agreed in the literature to yield higher PCA than rutile [9]. The anatase grain size observed for both coatings (12 and 16 nm) is of the same order but slightly higher, than the 8–10 nm reported by both Ma et al. and Choi et al. for TiO_2 sol–gel films onto 200 nm pore size alumina membranes [29,30]. N doping for the pipette and spiral bar applicator deposited coatings was <1 at.%. Interestingly, this sol–gel process gives rise to a mixed interstitial/substitutional N doping of TiO_2. There is disagreement in the literature regarding which dopant states are more effective at increasing PCA. Some authors indicate that interstitial N is better than substitutional N [19] whilst others give evidence that mixed substitutional/interstitial offers the optimum performance [18]. Peng et al. synthesised N doped TiO_2 powder by two different methods, which led to two different dopant states: interstitial N was achieved by a sol–gel method using urea as the nitrogen precursor, and substitutional N was obtained by annealing a TiO_2 powder under NH_3 flow. The nitrogen states were confirmed by XPS, with a peak at 396 eV for substitutional N, and a peak at 400 eV which they assigned to interstitial hyponitrite species ($N_2O_2^{2-}$). They found the interstitial N-doped TiO_2 had the highest PCA [19]. The justification of this behaviour was by Di Valentin et al. [67,68], who showed that in the case of substitutional doping the highest occupied level in the valence band would be the N 2p localized states, 0.14 eV above the top of the valence band, while for interstitial N doping the highest localized state would be the π^* character N–O state 0.73 eV above the valence band. Hu et al. attempted to make a distinction between bulk and surface doping, using a sol–gel method to produce a TiO_2 film which was uniformly doped in the surface and bulk, and a plasma treatment to obtain a film doped preferentially in the surface. The bulk-doped film showed interstitially doping, and the surface-doped film showed the presence of both interstitial and substitutional N. The surface-doped film showed the highest PCA and this was attributed to a higher concentration of nitrogen and oxygen vacancies at the surface, but this could also be a result of the combined presence of interstitial and substitutional N [18]. The sol–gel coatings deposited in this work show predominantly interstitial doping, but the exact nature of the interstitial doping (just N or N + NO) is not known, due to the N 1s 400 eV component possibly corresponding to surface contamination rather than NO doping. Nevertheless, the results from this study would indicate that mixed interstitial/substitutional doping (predominantly interstitial) can give rise to good photocatalytic performance.

The water permeability for the two sol–gel coated membranes

studied in this work was found to be reduced by approximately 50% in both cases due to the presence the sol gel coating on the membrane. In the previous work of Ma et al. and Choi et al., both groups repeated the sol–gel coating process to increase the sol–gel layer thickness and uniformity [29,30]. Ma et al., estimated that each initial coating cycle deposited layers of around 800 nm thick and reported that after two layers were deposited, the water permeability was reduced by 45% (no results given for a single layer) [29]. Choi et al. considered that each layer deposited has a thickness of approximately 300 nm and found that this layer lowered the water permeability by less than 10% [30]. In this work, from our EDX results it has been estimated that the average layer thickness for the spiral bar coated membrane is several hundreds of nanometres thick and this has led to a reduction in the water permeability by approximately 50%. Hence, compared to the work of Ma et al. and Choi et al., for nominally the same membrane, there is a greater reduction in the water permeability following the deposition of a single sol–gel layer [29,30]. Considering the different surface morphologies observed for the pipette and spiral bar applicator deposited coatings, it is rather surprising that there was little difference between the water permeabilities for the two different coating methods. It is clear why the spiral bar applicator deposited coating gives rise to a much reduced water permeability, as the passage of water is completely blocked by the 'islands' of the mud-cracked layer at the surface. There is no surface layer blockage effect for the pipette deposited coating as it penetrates the membrane more easily, but the results show that the sol–gel coating still reduces the water flow. In this case, the reduction in water permeability is occurring predominantly within the membrane bulk, rather than from the presence of a thick (but porous) surface layer, as seen for the spiral bar coated membrane. Possibly, at regions within the 200 nm pore membrane layer where the pore size is lower, the sol–gel becomes agglomerated, reducing the water flow.

Both the pipette and spiral bar applicator deposited coatings show high surface coverage, PCA and water permeability after a single layer has been deposited. Hence, although not studied in this work, there would appear to be little benefit from repeating the cycles of sol–gel deposition to grow a thicker layer. On the contrary, the water permeability will decrease, reducing the overall performance of a membrane based water treatment system. The mud-cracked morphology of the spiral bar applicator deposited coating allows the passage of water through the cracks, but compared to the more apparent conformal coverage of the pipette deposited coating, the limited contact area between the sol–gel coating and underlying membrane for the spiral bar applicator deposited coating would probably lead to a reduced durability of such a coated membrane during service. Hence, the pipette deposited N-doped TiO_2 sol–gel coated alumina membrane, with high surface coverage and good PCA under visible light, shows the most promise as a new photocatalytically active membrane based methodology for water treatment.

5. Conclusions

Alumina membranes with a nominal pore size of 200 nm have been coated with a N-doped TiO_2 sol–gel coating for photocatalytic purposes using two different sol–gel deposition methods. The uncoated and coated membranes have been characterised for their morphology, structure, composition. The PCA and water permeability have been determined. The following conclusions can be drawn from the work:

- Al_2O_3 membranes with 200 nm pore size show the presence of α-Al_2O_3 as the main crystallographic phase. Alumina particles ranging from sub-micron to a few micrometres in size form the basis of the filter top layer (about 4 μm in thickness). Smaller particles of tens to hundreds on nanometres in diameter decorate the larger particles and have been shown to be composed of ZrO_2 and a third phase of either a mixed Al/Zr oxide.
- The sol–gel N-doped TiO_2 coatings on 200 nm membranes deposited by pipette and spiral bar applicator have been extensively characterised. The two coatings are very similar in many respects. Both coatings exhibit a single crystal phase anatase structure with a N content of 0.9 at.% and same N doping states (predominantly interstitial N, with a smaller substitutional N contribution). There is a slight variation in the average grain size and coating coverage. The average grain size and coverage for the pipette deposited coatings is 12 nm and 85% respectively compared to 16 nm and 92% for the spiral bar applicator deposited coatings. There is however, a substantial difference in the morphology of the coatings. The spiral bar applicator deposited coatings exhibit a thicker mud-cracked surface layer with limited penetration of the porous membrane, whilst the pipette deposited coatings have mostly penetrated into the bulk of the membrane a thinner layer is present at the surface (which could not be clearly observed by SEM). It is considered that a difference in the sol–gel viscosity associated with the differing application methods is the cause of the observed variation in morphology.
- The PCA was determined through monitoring the degradation of CBZ under simulated solar radiation for a period of 120 min. For both N-doped TiO_2 sol–gel coated membranes, the PCA was found to be similar, being 58.6 ± 5.0% for the pipette deposited coating and 63.3 ± 3.9% for the spiral bar applicator deposited coating. The water permeability was observed to decrease by approximately 50% for both sol–gel coating methodologies, with the blockage occurring mostly at the membrane surface for the spiral bar applicator deposited coating and in the membrane bulk for the pipette deposited coating.
- The formation of a mud-cracked surface layer using the spiral bar applicator deposited coating allows the passage of water through the cracks, but results in a limited contact area between the coating and underlying membrane. The pipette deposited coating gives rise to a more conformal coverage of the membrane most probably leading to an increased durability of such a coated membrane during service. Hence, the pipette deposited N-doped TiO_2 sol–gel coated alumina membrane, with high surface coverage and good PCA under solar radiation, shows the most promise as a new photocatalytically active membrane based methodology for water treatment.

Acknowledgements

This work was supported by the European Commission's FP7 project NATIOMEM (245513-2). The authors are also grateful to Dr. P. Wilson for his assistance with AFM characterisation, Dr. G. Heinicke and Dr. A. Dorrit Enevoldsen for sourcing of the alumina membranes and discussions on coated membrane performance, and Professors J.E. Castle and R.A. Dorey for useful discussions.

References

[1] A.J. Frank, N. Kopidakis, J. van de Lagemaat, Electrons in nanostructured TiO_2 solar cells: transport, recombination and photovoltaic properties, Coord. Chem. Rev. 248 (2004) 1165–1179.
[2] I. Alessandri, E. Comini, E. Bontempi, G. Faglia, L.E. Depero, G. Sberveglieri, Cr-inserted TiO_2 thin films for chemical gas sensors, Sens. Actuat. B Chem. 128 (2007) 312–319.
[3] H.-J. Oh, J.-H. Lee, Y.-J. Kim, S.-J. Suh, J.-H. Lee, C.-S. Chi, Surface characteristics of porous anodic TiO_2layer for biomedical applications, Mater. Chem. Phys. 109 (2008) 10–14.
[4] H. Krüger, A. Hertwig, U. Beck, E. Kemnitz, Low temperature sol-gel metal

oxide and fluoride layer stacks for optical applications, Thin Solid Films 518 (2010) 6080–6086.
[5] M.A. Fox, M.T. Dulay, Heterogeneous photocatalysis, Chem. Rev. 93 (1993) 341–357.
[6] D.F. Ollis, H. Al-Ekabi, Photocatalytic Purification and Treatment of Water and Air Proceedings, Elsevier, Amsterdam, 1993.
[7] K. Tanaka, T. Hisanaga, A.P. Riviera, in: D.F. Ollis, H. Al-Ekabi (Eds.), Photocatalytic Purification and Treatment of Water and Air Proceedings, Elsevier, Amsterdam, 1993, pp. 169–178.
[8] A. Fujishima, X. Zhang, D.A. Tryk, TiO_2 photocatalysis and related phenomena, Surf. Sci. Rep. 63 (2008) 515–582.
[9] M.A. Henderson, A surface science perspective on TiO_2 photocatalysis, Surf. Sci. Rep. 66 (2011) 185–297.
[10] S. Sato, Photocatalytic activity of NO_x-doped TiO_2 in the visible light region, Chem. Phys. Lett. 123 (1986) 126–128.
[11] R. Asahi, T. Morikawa, T. Ohwaki, K. Aoki, Y. Taga, Visible-light photocatalysis in nitrogen-doped titanium oxides, Science 293 (2001) 269–271.
[12] R. Asahi, T. Morikawa, Nitrogen complex species and its chemical nature in TiO_2 for visible-light sensitized photocatalysis, Chem. Phys. 339 (2007) 57–63.
[13] Y. Nakano, T. Morikawa, T. Ohwaki, T. Taga, Deep-level optical spectroscopy investigation of N-doped TiO_2 films, Appl. Phys. Lett. 86 (2005), 132104–1-3.
[14] G.R. Torres, T. Lindgren, J. Lu, C.-G. Granqvist, S.-E. Lindquist, Photoelectrochemical study of nitrogen-doped titanium dioxide for water oxidation, J. Phys. Chem. B 108 (2004) 5995–6003.
[15] S. Livraghi, M.C. Paganini, E. Giamello, A. Selloni, C. Di Valentin, G. Pacchioni, Origin of photoactivity of nitrogen-doped titanium dioxide under visible light, J. Am. Chem. Soc. 128 (2006) 15666–15671.
[16] H. Irie, Y. Watanabe, K. Hashimoto, Nitrogen-concentration dependence on photocatalytic activity of $TiO_{2-x}N_x$ powders, J. Phys. Chem. B 107 (2003) 5483–5486.
[17] V.N. Kuznetsov, N. Serpone, On the origin of the spectral bands in the visible absorption spectra of visible-light-active TiO_2 specimens analysis and assignments, J. Phys. Chem. C 113 (2009) 15110–15123.
[18] S. Hu, F. Li, Z. Fan, The comparison of property and visible light activity between bulk and surface doped N-TiO_2 prepared by sol-gel and N_2-plasma treatment, Bull. Korean Chem. Soc. 33 (2012) 199–203.
[19] F. Peng, L. Cai, H. Yu, H. Wang, J. Yang, Synthesis and characterization of substitutional and interstitial nitrogen-doped titanium dioxides with visible light photocatalytic activity, J. Solid State Chem. 181 (2008) 130–136.
[20] M. Quiao, S. Wu, Q. Chen, J. Shen, Novel triethanolamine assisted sol-gel synthesis of N-doped TiO_2 hollow spheres, Mater. Lett. 64 (2010) 1398–1400.
[21] R.P. Bacsa, J. Kiwi, Effect of rutile phase on the photocatalytic properties of nanocrystalline titania during the degradation of p-coumaric acid, Appl. Catal. B 16 (1998) 19–29.
[22] G. Pecchi, P. Reyes, P. Sanhueza, J. Villaseñor, Photocatalytic degradation of pentachlorophenol on TiO_2 sol-gel catalysts, Chemosphere 43 (2001) 141–146.
[23] H. Yu, X. Zheng, Z. Yin, F. Tao, B. Fang, K. Hou, Preparation of nitrogen-doped TiO_2 nanoparticle catalyst and its catalytic activity under visible light, Chin. J. Chem. Eng. 15 (6) (2007) 802–807.
[24] M. Chekini, M.R. Mohammadizadeh, S.M. Vaez Allaei, Photocatalytic and superhydrophilicity properties of N-doped TiO_2 nanothin films, Appl. Surf. Sci. 257 (2011) 7179–7183.
[25] T. Ohno, Preparation of visible light active S-doped TiO_2 photocatalysts and their photocatalytic activities, Water Sci. Technol. 49 (4) (2004) 159–163.
[26] J. Nieto, J. Freer, D. Contreras, R.J. Candal, E.E. Sileo, H.D. Mansilla, Photocatalyzed degradation of flumequine by doped TiO_2 and simulated solar light, J. Hazard. Mater. 155 (2008) 45–50.
[27] M. Factorovich, L. Guz, R. Candal, N-TiO_2: chemical synthesis and photocatalysis, Adv. Phys. Chem. (2011) 8. ID: 821204.
[28] R. Azouani, A. Michau, K. Hassouni, K. Chhor, J.F. Bocquet, J.L. Vignes, A. Kanaev, Elaboration of pure and doped TiO_2 nanoparticles in sol-gel reactor with turbulent micromixing: application to nanocoatings and photocatalysis, Chem. Eng. Res. Des. 88 (2010) 1123–1130.
[29] N. Ma, X. Quan, Y. Zhang, S. Chen, H. Zhao, Integration of separation and photocatalysis using an inorganic membrane modified with Si-doped TiO_2 for water purification, J. Membr. Sci. 335 (2009) 58–67.
[30] H. Choi, E. Stathos, D. Dionysiou, Sol-gel preparation of mesoporous photocatalytic TiO_2 films and TiO_2/Al_2O_3 composite membranes for environmental applications, Appl. Catal. B Environ. 63 (2006) 60–67.
[31] S. Castiglioni, R. Bagnati, R. Fanelli, F. Pomati, D. Calamari, E. Zuccato, Removal of pharmaceuticals in sewage treatment plants in Italy, Environ. Sci. Technol. 40 (2006) 357–363.
[32] X.S. Miao, J.J. Yang, C.D. Metcalfe, Carbamazepine and its metabolites in wastewater and in biosolids in a municipal wastewater treatment plant, Environ. Sci. Technol. 39 (2005) 7469–7475.
[33] T. Reemtsma, S. Weiss, J. Mueller, M. Petrovic, S. Gonzalez, D. Barcelo, F. Ventura, T.P. Knepper, Polar pollutants entry into the water cycle by municipal wastewater: a European perspective, Environ. Sci. Technol. 40 (2006) 5451–5458.
[34] L. Dsikowitzky, J. Schwarzbauer, R. Littke, The anthropogenic contribution to the organic load of the Lippe River (Germany). Part II: quantification of specific organic contaminants, Chemosphere 57 (2004) 1289–1300.
[35] C. Tixier, H.P. Singer, S. Oellers, S.R. Muller, Occurrence and fate of carbamazepine, clofibric acid, diclofenac, ibuprofen, ketoprofen, and naproxen in surface waters, Environ. Sci. Technol. 37 (2003) 1061–1068.
[36] S. Wiegel, A. Aulinger, R. Brockmeyer, H. Harms, J. Loffler, H. Reincke, R. Schmidt, B. Stachel, W. Tumpling, A. Wanke, Pharmaceuticals in the river Elbe and its tributaries, Chemosphere 57 (2004) 107–126.
[37] R. Fenz, A.P. Blaschke, M. Clara, H. Kroiss, D. Mascher, M. Zessner, Quantification of sewer exfiltration using the anti-epileptic drug carbamazepine as marker species for wastewater, Water Sci. Technol. 52 (2005) 209–217.
[38] J.E. Drewes, T. Heberer, T. Rauch, K. Reddersen, Fate of pharmaceuticals during ground water recharge, Groundw. Monit. Remediat. 23 (2003) 64–72.
[39] T.J. Scheytt, P. Mersmann, T. Heberer, Mobility of pharmaceuticals carbamazepine, diclofenac, ibuprofen, and propyphenazone in miscible-displacement experiments, J. Contam. Hydrol. 83 (2006) 53–69.
[40] T. Heberer, A. Mechlinski, B. Fanck, A. Knappe, G. Massmann, A. Pekdeger, B. Fritz, Field studies on the fate and transport of pharmaceutical residues in bank filtration, Groundw. Monit. Remediat. 24 (2004) 70–77.
[41] M. Kahle, I.J. Buerge, M.D. Muller, T. Poiger, Hydrophilic antropogenic markers for quantification of wastewater contamination in ground- and surface waters, Environ. Toxicol. Chem. 28 (2009) 2528–2536.
[42] T.A. Ternes, M. Meisenheimer, D. McDowell, F. Sacher, H.J. Brauch, B. Haist-Gulde, G. Preuss, U. Wilme, N. Zulei- Seibert, Removal of pharmaceuticals during drinking water treatment, Environ. Sci. Technol. 36 (2002) 3855–3863.
[43] T.J. Scheytt, P. Mersmann, T. Heberer, Mobility of pharmaceuticals carbamazepine, diclofenac, ibuprofen, and propyphenazone in miscible-displacement experiments, J. Contam. Hydrol. 83 (2006) 53–69.
[44] M. Clara, B. Strenn, N. Kreuzinger, Carbamazepine as a possible anthropogenic marker in the aquatic environment: investigations on the behaviour of carbamazepine in wastewater treatment and during groundwater infiltration, Water Res. 38 (2004) 947–954.
[45] D. Vogna, R. Marotta, R. Andreozzi, A. Napolitano, M. d'Ischia, Kinetic and chemical assessment of the UV/H_2O_2 treatment of antiepileptic drug carbamazepine, Chemosphere 54 (2004) 497–505.
[46] R. Fenz, A.P. Blaschke, M. Clara, H. Kroiss, D. Mascher, M. Zessner, Quantification of sewer exfiltration using the anti-epileptic drug carbamazepine as marker species for wastewater, Water Sci. Technol. 52 (2005) 209–217.
[47] D. Avisar, I. Horovitz, L. Lozzi, F. Ruggeri, M. Baker, M.A. Abel, H. Mamane, Impact of water quality on removal of carbamazapine in natural waters by TiON photo-catalytic thin film surfaces, J. Hazard. Mater. 244–245 (2013) 463–471.
[48] C. Massaro, M.A. Baker, F. Cosentino, P.A. Ramires, S. Klose, E. Milella, Surface and biological evaluation of hydroxyapatite-based coatings on titanium deposited by different techniques, J. Biomed. Mater. Res. 58 (2001) 651–657.
[49] S.-H. Lee, E. Yamasue, H. Okumura, K.N. Ishihara, Preparation of N-doped TiO_x films as photocatalyst using reactive sputtering with dry air, Mater. Trans. 50 (2009) 1805–1811.
[50] Z.G. Li, S. Miyake, Characteristics of N-doped TiO_2 thin films grown on unheated glass substrate by inductively coupled plasma assisted dc reactive magnetron sputtering, Appl. Surf. Sci. 255 (2009) 9149–9153.
[51] L. Mi, P. Xu, P.N. Wang, Experimental study on the bandgap narrowings of TiO_2 films calcined under N_2 or NH_3 atmosphere, Appl. Surf. Sci. 255 (2008) 2574–2580.
[52] O. Diwald, T.L. Thompson, T. Zubkov, E.G. Goralski, S.D. Walck, J.T. Yates Jr., Photochemical activity of nitrogen-doped rutile TiO_2(110) in visible light, J. Phys. Chem. B 108 (2004) 6004–6008.
[53] I. Takahashi, D.J. Payne, R.G. Palgrave, R.G. Egdell, High resolution x-ray photoemission study of nitrogen doped TiO_2 rutile single crystals, Chem. Phys. Lett. 454 (2008) 314–317.
[54] M. Batzill, E.H. Morales, U. Diebold, Surface studies of nitrogen implanted TiO_2, Chem. Phys. 339 (2007) 36–43.
[55] S.H. Cheung, P. Nachimuthu, A.G. Joly, M.H. Engelhard, M.K. Bowman, S.A. Chambers, N incorporation and electronic structure in N-doped TiO_2(110) rutile, Surf. Sci. 601 (2007) 1754–1762.
[56] H. Matsui, H. Tabata, N. Hasuike, H. Harima, B. Mizobuchi, Epitaxial growth and characteristics of N-doped anatase TiO_2 films grown using a free-radical nitrogen oxide source, J. Appl. Phys. 97 (12) (2005), 123511–1-8.
[57] H.M. Yates, M.G. Nolan, D.W. Sheel, M.E. Pemble, The role of nitrogen doping on the development of visible light-induced photocatalytic activity in thin TiO_2 films grown on glass by chemical vapour deposition, J. Photochem. Photobiol. A Chem. 179 (2006) 213–223.
[58] M.A. Baker, H. Fakhouri, R. Grilli, J. Pulpytel, W. Smith, F. Arefi-Khonsari, Effect of total gas pressure and O_2/N_2 flow rate on the nanostructure of N-doped TiO_2 thin films deposited by reactive sputtering, Thin Solid Films 552 (2014) 10–17.
[59] T. Herranz, X. Deng, A. Cabot, Z. Liu, M. Salmeron, In situ XPS study of the adsorption and reactions of NO and O_2 on gold nanoparticles deposited on TiO_2 and SiO_2, J. Catal. 283 (2011) 119–123.
[60] K. Obata, H. Irie, K. Hashimoto, Enhanced photocatalytic activities of Ta, N co-doped TiO_2 thin films under visible light, Chem. Phys. 339 (2007) 124–132.
[61] B. Liu, L. Wen, X. Zhao, The structure and photocatalytic studies of N-doped TiO_2 films prepared by radio frequency reactive magnetron sputtering, Sol. Energy Mat. Sol. C 92 (2008) 1–10.
[62] M.-H. Chan, F.-H. Lu, characterization of N-doped TiO_2 films prepared by reactive sputtering using air/Ar mixtures, Thin Solid Films 518 (2009) 1369–1372.
[63] Jin Wang, D.N. Tafen, J.P. Lewis, Z. Hong, A. Manivannan, M. Zhi, M. Li, N. Wu, Origin of photocatalytic activity of nitrogen-doped TiO_2 nanobelts, J. Am.

Chem. Soc. 131 (2009) 12290–12297.
[64] M. Sathish, B. Viswanathan, R.P. Viswanath, C.S. Gopinath, Synthesis, characterization, electronic structure, and photocatalytic activity of nitrogen-doped TiO_2 nanocatalyst, Chem. Mater. 17 (2005) 6349–6353.
[65] J. Sun, L. Qiao, S. Sun, G. Wang, Photocatalytic degradation of orange G on nitrogen-doped TiO_2 catalysts under visible light and sunlight irradiation, J. Hazard. Mater. 155 (2008) 312–319.
[66] A. de Oliveira-Sousa, M.A.S. da Silva, S.A.S. Machado, L.A. Avaca, P. de Lima-Neto, Influence of the preparation method on the morphological and electrochemical properties of Ti/IrO_2-coated electrodes, Electrochim. Acta 45 (2000) 4467–4473.
[67] C. Di Valentin, G. Pacchioni, A. Selloni, S. Livraghi, E. Giamello, Characterization of paramagnetic species in N-doped TiO_2 powders by EPR spectroscopy and DFT calculations, J. Phys. Chem. B 109 (2005) 11414–11419.
[68] C. Di Valentin, G. Pacchioni, A. Selloni, Origin of the different photoactivity of N-doped anatase and rutile TiO_2, Phys. Rev. B 70 (2004), 085116-1-4.